

TACE: A unified Irreducible Cartesian Tensor Framework for Atomistic Machine Learning

Zemin Xu^{1,2}, Wenbo Xie^{1*}, Daiqian Xie², P. Hu^{1,3*}

¹School of Physical Science and Technology, ShanghaiTech University, Shanghai, 201210, China.

²State Key Laboratory of Coordination Chemistry, Key Laboratory of Mesoscopic Chemistry of MOE, School of Chemistry and Chemical Engineering, Nanjing University, Nanjing, 210023, China.

³School of Chemistry and Chemical Engineering, The Queen’s University of Belfast, Belfast, BT9 5AG, UK.

*Corresponding author(s). E-mail(s): xiewb1@shanghaitech.edu.cn; p.hu@qub.ac.uk, hupj@shanghaitech.edu.cn;

Contributing authors: xvzemin@smail.nju.edu.cn;

Abstract

Machine learning has transformed atomistic simulations and materials science, yet most existing approaches rely on spherical-tensor representations. Here, we introduce the Tensor Atomic Cluster Expansion (TACE), a unified framework formulated entirely in Cartesian space, enabling systematic and consistent prediction of arbitrary structure-dependent tensorial properties. TACE achieves this by decomposing atomic environments into a complete hierarchy of irreducible Cartesian tensors, ensuring symmetry-consistent representations that naturally encode invariance and equivariance constraints. Beyond geometry, TACE incorporates universal embeddings that flexibly integrate diverse attributes including computational levels, charges, magnetic moments and field perturbations. This allows explicit control over external invariants and equivariants in the prediction process. Long-range interactions are also accurately described through the Latent Ewald Summation module within the short-range approximation, providing a rigorous yet computationally efficient treatment of electrostatic and dispersion effects. We demonstrate that TACE attains accuracy, stability, and efficiency on par with or surpassing leading equivariant frameworks across finite molecules and extended materials. This includes in-domain and out-of-domain benchmarks, spectra, Hessian, external-field responses, charged and magnetic systems, multi-fidelity training, heterogeneous catalysis, and even superior performance within the uMLIP benchmark. Crucially, TACE bridges scalar and tensorial modeling and establishes a Cartesian-space paradigm that unifies and extends beyond the design space of spherical-tensor-based methods. This work lays the foundation for a new generation of universal atomistic machine learning models capable of systematically capturing the rich interplay of geometry, fields and material properties within a single coherent framework.

1 Introduction

Atomistic simulations rely on accurate potential energy surfaces (PES) to describe structures, dynamics, and reactions across molecules and materials. While density functional theory (DFT) is the reliability reference, $\mathcal{O}(N^3)$ or higher scaling limits the accessibility of atomistic simulations to large spatial and temporal scales and to complex chemical reactions, motivating machine learning interatomic potentials (MLIPs) as practical surrogates. Recent equivariant models have markedly advanced data efficiency and accuracy by learning from ab initio energies, forces, and stresses (E/F/S); yet can still yield limited fidelity in downstream physical property predictions despite low test errors when essential physical constraints are not included [1] or when the models show poor extrapolation and robustness [2]. Many physically meaningful quantities that are readily available from ab initio calculations, such as charges, magnetic moments, and external fields, are often underutilized or not effectively integrated into state-of-the-art (SOTA) models, which prevents one from realistic, cross-validated modeling and gleaning more insights.

Various physical constraints and conservation laws can provide critical information to assist the prediction of complex reaction systems. For quantities such as forces, which are explicitly derived from conservative field, it is essential to respect the underlying physical constraints to ensure a smoothly varying and physically meaningful landscape. In practice, direct-force learning (e.g., direct-force pretraining [1]) can be helpful, but robust and accurate prediction ultimately hinges on conservative training and physics-aware supervision. In electrocatalysis, applied potentials and external fields shift adsorption energies, stabilizing or destabilizing transition states, and altering reaction kinetics and spectroscopic responses; models that do not explicitly encode external fields and long-range interaction can fit forces yet yield physically incorrect conclusions. Likewise, magnetic materials are intrinsically $6N$ -dimensional rather than $3N$ (see SI Fig. S1, so restricting supervision to E/F/S is insufficient for accurate predictions. These considerations motivate going beyond (E/F/S) alone and integrating additional degrees of freedom and constraints to improve accuracy, stability, and transferability, which will tremendously benefit the understanding of complicated chemical systems.

To be universal, the model needs to handle both invariant and equivariant properties within a single, shared, symmetry-consistent framework, learning scalar representations for invariant quantities together with tensor representations for equivariant outputs (conserved quantities such as forces, stresses, polarization, polarizabilities; and direct properties such as direct-forces, direct-stresses, direct-dipoles, and direct-polarizabilities), so that all heads obey the expected behavior and can be co-supervised for mutual consistency.

MLIPs typically decompose the total energy into atomic site energies, which depend on the local environment of individual atoms. Early generations often relied on fixed hand-crafted representations and simple Cartesian neural networks that mapped atomic coordinates and species into invariant features. These invariant approaches achieved considerable success by ensuring translational, rotational, and permutational invariance [3–7]. However, they were fundamentally limited in accuracy and their ability to capture tensorial physical quantities. The advent of equivariant message passing neural networks marked a major breakthrough. By incorporating irreducible representations of the $O(3)$ group via spherical tensors, models such as NequIP, Allegro and MACE [8–10] introduced physics-informed inductive biases that significantly improved data efficiency and generalization. This shift revolutionized the field and made spherical-tensor-based methods the mainstream choice. Nevertheless, spherical tensor formulations present intrinsic challenges. The use of Clebsch-Gordan (CG) coefficients to couple angular momenta incurs substantial computational cost (the $SO(2)$ tensor product [11] will be discussed later). Moreover, spherical tensors are defined with respect to a fixed axis, commonly the z axis, which introduces directional bias [12, 13]. In parallel, Cartesian tensor approaches have experienced a resurgence as attractive alternatives. TensorNet [14], HotPP [15], CACE [16], and CAMP [17] explored feature construction directly in Cartesian space. These models rely on reducible Cartesian tensors and aimed to improve either accuracy or computational efficiency compared to spherical-tensor-based methods. They indeed achieved some progress, particularly in low rank cases where Cartesian tensor contractions are generally faster. However, their accuracy has typically not surpassed that of models built on irreducible spherical tensor representations. TensorNet is restricted to rank-2 tensor and lacks systematic mechanisms for higher body interactions. HotPP [15] introduced deeper message passing and gating in Cartesian space but relied on reducible tensors with redundant representations. CACE encodes many body correlations explicitly but is limited in parameterization flexibility. CAMP [17] enforced strict permutation symmetry but did not guarantee tracelessness. In fact, irreducible tensors also exist in Cartesian space. Unlike spherical tensors, they do not privilege any orientation, and their tensor products are often simpler and more computationally efficient up to rank four [13]. ICTP [13], although pioneering the use of irreducible

Cartesian tensors to achieve accuracies comparable to spherical tensors, requires explicit permutation of all indices in tensor products, and its implementation is limited to rank-3 tensors. Moreover, their representation cannot exploit lower-weight Cartesian tensors, thereby not fully realizing the potential of the Cartesian framework.

Here, we introduce the Tensor Atomic Cluster Expansion (TACE), a SOTA framework designed to address these challenges by unifying scalar and tensorial modeling entirely within Cartesian space. TACE systematically decomposes atomic environments into (irreducible) Cartesian tensors, ensuring exact symmetry consistency while avoiding the axis-dependence and CG overhead inherent to spherical-tensor-based methods. Building on this representation, TACE provides universal embeddings on both sides: (i) invariant embeddings for graph or node-level scalars (e.g., charges, fidelity tags, spin multiplicity) and (ii) equivariant embeddings for tensors (e.g., external fields, non-collinear magnetic moments) injected into the same feature space so that both predicted quantities and embedded quantities are handled on equal footing, enabling explicit control during the prediction process. A Latent Ewald Summation (LES) [18–21] plug-in further supplies a rigorous yet efficient route to long-range interactions within the same training loop. We perform comprehensive evaluations across in-domain and out-of-domain molecular sets, condensed-phase liquids, field-perturbed solids, charged and magnetic materials, reactions systems in heterogeneous catalysis and universal MLIP benchmarks, to assess TACE’s ability to integrate diverse physical information, both simultaneously and independently, to improve prediction accuracy. Across this breadth, TACE delivers accuracy on par with or surpassing that of leading methods, while providing a systematic and extensible paradigm for modeling the complex interplay between geometry, fields, and material properties.

2 Results

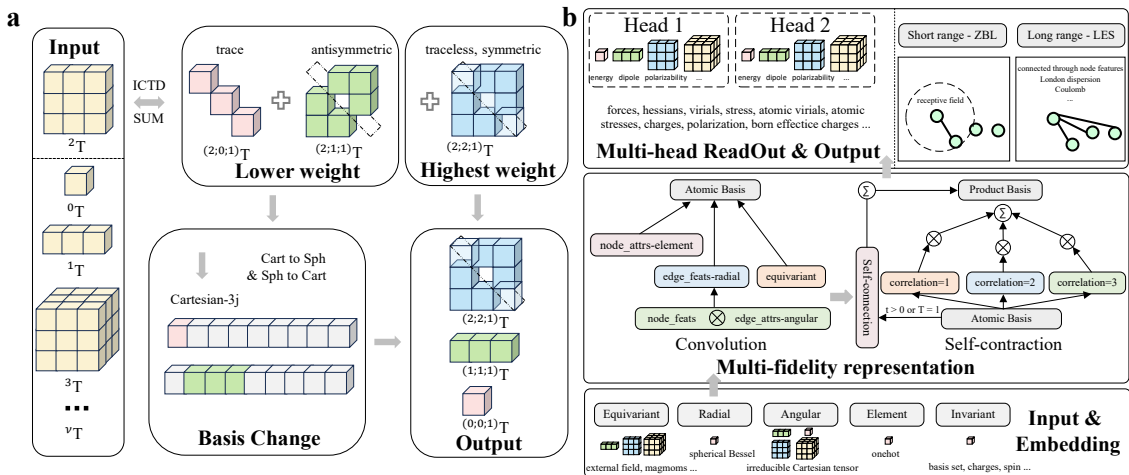


Fig. 1: Irreducible Cartesian tensor and the TACE architecture. **a** Taking the rank-2 case as an example, ICTD can extract the corresponding irreducible components with respect to a given weight. Through the basis transformation between Cartesian and spherical basis, the lower-weight parts of Cartesian tensors can be converted to “rank = weight”. **b** Illustration of the overall data flow in TACE. The embeddings of invariants and equivariants are generic. In this work we demonstrate embeddings for different computational levels, charges, external fields, and magnetic moments, but in principle other quantities are also supported. We also support the use of ZBL [22] and Latent Ewald Summation [18–21] as plugins.

2.1 The TACE architecture

The feature learning of TACE begins with the construction of a graph in which each node is parameterized by learned irreducible Cartesian tensors (ICTs) \mathbf{h}_i that encode its chemical environment. For each edge, a one-particle basis ϕ_{ij} is computed and to obtain permutation-invariant representations of semi-local environments, a pooling operation is applied to aggregate these local features, resulting in the so-called atomic basis \mathbf{A}_i . Building on this, higher-body-order features are systematically constructed through

tensor contraction over the \mathbf{A}_i , yielding a product basis \mathbf{B}_i that captures $(n + 1)$ -body interactions. TACE follows the framework of Atomic Cluster Expansion (ACE) [10, 23–26], while acknowledging that various alternative design choices remain available. In addition to the aforementioned parts, some extra features have also been added, as shown in Fig. 1b.

2.2 Cartesian tensor

A generic Cartesian tensor of rank- ν , denoted as ${}^\nu\mathbf{T}$, is a multilinear object with 3^ν components defined in a three-dimensional Euclidean space. The term “**generic Cartesian tensor**” refers to one with no imposed symmetry or traceless constraints among its indices. These components transform according to specific representation rules under the action of the orthogonal group $O(3)$, which includes both rotations and spatial inversions in three-dimensional space. In general, such tensors are reducible under $O(3)$, meaning that they can be decomposed into a direct sum of irreducible components, each associated with a definite angular momentum character ℓ . A generic Cartesian tensor ${}^\nu\mathbf{T}$ can be expressed as a sum of ICTs of the same rank but different weight ℓ (note that this “weight” is not the “learning weight” in machine learning):

$${}^\nu\mathbf{T} = \sum_{\ell, q} ({}^{\nu; \ell; q})\mathbf{T} \quad (1)$$

where each $({}^{\nu; \ell; q})\mathbf{T}$ is an irreducible component of rank- ν , weight ℓ with $2\ell + 1$ freedom, corresponding to a spherical tensor of degree ℓ and q denotes the label (since the multiplicity for given ν and ℓ may be greater than 1). As a result, the generic Cartesian tensor includes all possible irreducible parts from weight $\ell = 0$ up to $\ell = \nu$. This decomposition reveals that Cartesian tensors consist of a mixture of physical components: scalar parts ($\ell = 0$), vector parts ($\ell = 1$), and higher-rank fully symmetric-traceless tensors ($\ell \geq 2$), each transforming independently under rotation or inversion and corresponding to an invariant subspace of the tensor representation space.

2.3 Irreducible Cartesian tensor decomposition

As is well known, a generic rank-2 Cartesian tensor \mathbf{T} can be decomposed into its irreducible components as follows (see also Fig. 1a):

$$\mathbf{T}_{ij} = \left(\underbrace{\frac{1}{2}(\mathbf{T}_{ij} + \mathbf{T}_{ji}) - \frac{1}{3}\delta_{ij}\mathbf{T}_{kk}}_{\ell=2} \right) + \left(\underbrace{\frac{1}{2}(\mathbf{T}_{ij} - \mathbf{T}_{ji})}_{\ell=1} \right) + \left(\underbrace{\frac{1}{3}\delta_{ij}\mathbf{T}_{kk}}_{\ell=0} \right) \quad (2)$$

This decomposition yields the rank-2 tensor’s irreducible components corresponding to angular momenta $\ell = 2$, $\ell = 1$, and $\ell = 0$. Generalizations to higher-rank tensors with $\nu = 3, 4, 5$ (numerical or analytical) were proposed in 1965, 1982, and 2024, respectively [27–29]. These ICTs could be obtained via irreducible Cartesian tensor decomposition (ICTD) matrices. We denote the ICTD operator and its associated decomposition matrix as \mathcal{T} [30]. Although it is possible to compute ICTs with rank $\nu > 5$ using numerical methods, such approaches are not suitable for use in the forward pass of deep learning models, as they significantly degrade computational efficiency and as far as we know, there are no models utilizing numerical methods for this operation now. In fact, decomposition matrices were previously only available up to rank $\nu = 5$, and their generation has traditionally been computationally expensive. However, thanks to the recent work of Shihao Shao [30], analytical ICTD matrices for $\nu > 5$ can now be efficiently constructed. The overall decomposition can be written as follows, where $\text{vec}(\cdot)$ denotes flattening of the Cartesian tensor and the symbol \triangleright denotes an operation applied to the operand on its right-hand side.

$$\text{vec} \left(({}^{\nu; \ell; q})\mathbf{T} \right) = ({}^{\nu; \ell; q})\mathcal{T} \triangleright \text{vec} \left({}^\nu\mathbf{T} \right) \quad (3)$$

In fact, we also implemented symmetrized tensors and recursive tracelessness to obtain irreducible Cartesian tensors, which works also for arbitrary Cartesian tensors. However, this approach is ultimately purely numerical, and ICTD provides a more systematic analytical alternative.

2.3.1 Equivariant operation

The model architecture is primarily composed of two types of equivariant operations.

The first type, tensor contraction maps two tensors ${}^{\nu_1}\mathbf{T}$ and ${}^{\nu_2}\mathbf{T}$ to a new tensor ${}^{\nu_3}\mathbf{T}$ whose rank $\nu_3 = \nu_1 + \nu_2 - 2k$ is determined by the number of contracted indices k , where $0 \leq k \leq \min(\nu_1, \nu_2)$.

When no indices are contracted, the operation is equivalent to tensor product. Eqn. 4 gives the element-wise expression of the tensor contraction, which may be abbreviated as ${}^{\nu_3}\mathbf{T} = {}^{\nu_1}\mathbf{T} \otimes_{(\nu_1, \nu_2, \nu_3)} {}^{\nu_2}\mathbf{T}$. In practice, certain constants such as $3^{-\frac{k}{2}}$ can be used to modulate the variance.

$${}^{\nu_1 + \nu_2 - 2k}\mathbf{T}_{a_1 \dots a_{\nu_1 - k} b_1 \dots b_{\nu_2 - k}} = \sum_{i_1, \dots, i_k} {}^{\nu_1}\mathbf{T}_{a_1 \dots a_{\nu_1 - k} i_1 \dots i_k} {}^{\nu_2}\mathbf{T}_{i_1 \dots i_k b_1 \dots b_{\nu_2 - k}} \quad (4)$$

We observe that for a given combination (ν_1, ν_2, ν_3) , there can be multiple distinct ways to perform contractions, each corresponding to a different contraction path. Drawing inspiration from e3nn [31], we define each such distinct contraction configuration as a path. Specifically, if k indices are contracted between the first and second tensors, the number of possible paths can be computed without considering any symmetries. It equals the number of ways to select k contracted indices from the first tensor and k contracted indices from the second tensor, multiplied by the number of permutations of these k indices. Since Cartesian tensors correspond to reducible representations and therefore contain redundant information, Cartesian-based-tensor-contraction models [15, 17] typically include only a single path for each combination and may directly embedding radial information to edge. In contrast, by employing ICTD, we have the flexibility to switch between irreducible and reducible Cartesian tensors. In the irreducible representation, the paths are often symmetric, allowing us to select only one of them, though better selection schemes may be developed in the future. We then assign a radial-dependent weight to each.

It is well known that including or not including inversion operations distinguishes the $\text{SO}(3)$ and $\text{O}(3)$ groups. If inversion is not considered (i.e., only $\text{SO}(3)$ is taken into account), all spherical harmonics are assumed to have even parity within the framework of e3nn [31]. When parity is taken into account, the spherical harmonics alternate between even (e) and odd (o) parity. For models such as NequIP [8], there is an option to enable parity. Enabling parity allows the model to retain more intermediate irreducible components, but it has little effect on accuracy, which primarily depends on L_{\max} or ℓ_{\max} . Considering $\text{O}(3)$ implies that the model internally handles polar and pseudotensors separately. In Cartesian space, the angular basis (Cartesian harmonics) in Eqn. 11 transforms in the same way as spherical harmonics. If pseudotensor prediction is required, there are two approaches:

1. Follow the e3nn [31] implementation and explicitly mark parity.
2. Convert between polar and pseudovectors by contracting tensors with the Levi-Civita tensor ε_{ijk} . For example, if we want to obtain a pseudovector from two polar vectors:

$$({}^1\mathbf{T}_1 \otimes {}^1\mathbf{T}_2)_i = \varepsilon_{ijk} ({}^1\mathbf{T}_1)_j ({}^1\mathbf{T}_2)_k \quad (5)$$

The second type of operation consists of linear combinations of tensors with identical rank ν , resulting in new tensors of the same rank. Specifically, given \tilde{c} input tensors ${}^{\nu}\tilde{\mathbf{T}}$, we can construct c output tensors ${}^{\nu}{}_c\mathbf{T}$ of the same rank through a learnable linear transformation. This operation can be interpreted as treating each tensor as a neuron, thereby enabling linear operations to be applied. In fact, similar to approaches such as NequIP and HotPP [8, 15], one could introduce nonlinearity via gating to construct multi-layer perceptrons (MLPs) for tensor with $\nu > 0$.

2.3.2 Element embedding

In the TACE framework, we denote node features by ${}^{\nu_1}{}_c\mathbf{h}_i^{(t)}$, where i refers to the atom index, $\nu_1 \in L_{\max}$ indicates the tensor rank, p indexes the contributing paths, c denotes the feature channel, and t represents the layer index. The rank-0 node features are initialized by applying a linear transformation to the one-hot encoding of the atomic species. Higher-rank node features are subsequently constructed via tensor contraction involving edge attributes. Node features will be iteratively updated through convolution across successive layers. The prevailing MLIPs predominantly adopt one-hot encoding to scalar features for reasons analogous to those in large language models (LLMs). Elements are not entirely independent, and those within the same period or group often exhibit similar properties. This correlation allows the learned element embeddings to be linearly reduced in dimensionality and visualized after training, thereby revealing underlying relationships.

2.3.3 Universal invariant embedding

Here, we proposed the incorporation of additional graph- or node-level invariant physical quantities such as charges and computational levels. For discrete element-like properties, we employ one-hot encoding

followed by a linear layer, while for continuous properties we adopt an MLP-based embedding. All non-element invariant embeddings are concatenated and then projected into the channel dimension. We denote this combined representation as universal invariant features, which is then directly added to the node features. This embedding approach allows us to incorporate any invariant quantity that can reasonably influence the PES. By embedding these properties, the model gains additional descriptive flexibility for the PES, thereby improving its accuracy and transferability across different chemical environments.

Discrete embedding — Multi-fidelity: In general, due to the computational cost of high accuracy computational level, MLIPs are often constructed at a reasonably chosen lower level of theory. However, a variety of approaches such as Δ -learning, MFML, o-MFML, and MF Δ ML [32] have been proposed to leverage abundant low fidelity data together with a limited amount of high fidelity data. This is commonly referred to as multi-fidelity training, where the term fidelity denotes the accuracy of the quantum chemistry method. These approaches typically aim to correct PES from low fidelity to high fidelity. Nevertheless, we argue that such methods remain insufficiently elegant. As an illustrative example, we consider the embedding of the same functional with different basis sets as a discrete variable to demonstrate the effectiveness of the universal invariant embedding. Although not tested in this work, we anticipate that the method can also be applied to other invariants that affect the PES. In the following description, if the model is trained on datasets of multiple fidelities unified within a single model, it is referred to as MFTACE.

Continuous embedding — Charges: For continuous variables, such as charges or the total charge, the embedding is performed in the same manner as described above and will not be elaborated further here.

2.3.4 Universal equivariant embedding

Meanwhile, we propose a general scheme for embedding equivariant physical quantities within the ACE framework. This approach is universally applicable to other ACE-based models, allowing any physically meaningful equivariant feature to be incorporated into the representation. Strictly speaking, **pseudovectors** need to be considered within the $O(3)$ framework and should be embedded in the corresponding irreducible components. Additionally, if **time-reversal** symmetry is taken into account, our treatment needs to be modified accordingly; however, from a numerical perspective, fitting remains feasible.

External electric field: The diverse responses of materials to external stimuli, ranging from linear to nonlinear and coupled effects, are crucial in determining the functional properties of a wide range of systems, including dielectrics, ferroelectrics, multiferroics, and piezoelectrics. Taking the external electric field as a representative example, we illustrate how such a field can be embedded into models based on ACE. Under universal equivariant embeddings, the \mathbf{A} -basis in Eqn. 11 is modulated by element- and channel-dependent weights w_{c,z_i} , together with optional statistical information σ about the field. This operation is applied after constructing the atomic basis and before forming the product basis. The atomic basis under an external electric field is then given by:

$$\underbrace{{}^1\mathbf{A}_i^{(t)}}_{\text{ext}} = {}^1\mathbf{A}_i^{(t)} + w_{c,z_i} \cdot \frac{{}^1\mathbf{E}_{\text{ext}}}{\sigma} \quad (6)$$

Magnetic moments: Similarly, the embedding scheme can be applied to both collinear and non-collinear magnetism. It is important to emphasize that the physical symmetries associated with spin degrees of freedom differ between the two cases. In non-collinear cases, geometric tensors transform according to $SO(3)$ under spatial rotations, while spinors transform according to $SU(2)$, with these transformations intricately coupled. In contrast, collinear cases define a global spin axis, rendering the transformations of atomic positions and spins effectively separable. Therefore, in principle, spins in collinear setups should be treated as scalars. For non-collinear setups, the overall procedure remains essentially the same as in the presence of an external field, with the main distinction that the magnetic moments are treated for each atom.

2.3.5 Radial embedding

The spherical Bessel functions of the first kind, j_n , as proposed in DimeNet [33] are complete sets of orthogonal polynomials, and are therefore well-suited as radial basis functions. In this work, we adopt

j_0 and construct the radial basis using its zeros. The corresponding expression is given by:

$$j_0^n(r_{ij}) = \sqrt{\frac{2}{c}} \frac{\sin(\frac{n\pi}{c} r_{ij})}{r_{ij}} f_{\text{cut}}(r_{ij}) \quad (7)$$

The edge length $r_{ij} = \|\mathbf{r}_{ij}\|$ is first expanded using a set of radial basis functions and subsequently multiplied by an envelope cutoff function to ensure the smoothness of the PES. By tuning the hyperparameters of polynomial basis, we can effectively control the decay behavior of atomic contributions. Further details can be found in the work of ref. [33]. The resulting radial embeddings are subsequently passed through MLPs to generate path weights. We also implement j_n of any order in the code. In our trials, using the first few orders did not result in a significant improvement or degradation of performance, though it may prove useful in future applications.

$$R_{p_1 c \nu_1 \nu_2 \nu_3}^{(t)}(r_{ij}) = \text{MLP} \left(j_0^n(r_{ij}) \right) \quad (8)$$

2.3.6 Angular embedding

The angular information of an atomic environment are encoded in the normalized edge vector, $\hat{\mathbf{r}}_{ij} = \mathbf{r}_{ij}/r_{ij}$. In contrast to most of the SOTA models which rely on projections onto spherical harmonics, we adopt a cartesian representation. Specifically, we construct edge attributes ${}^{(\nu_2; \nu_2; 1)} \mathbf{E}_{ij}$, where $\nu_2 \in \ell_{\max}$ as:

$${}^{(\nu_2; \nu_2; 1)} \mathbf{E}_{ij} = \frac{(2\nu_2 - 1)!!}{\nu_2!} \cdot {}^{(\nu_2; \nu_2; 1)} \mathcal{G}_{\triangleright} \left(\underbrace{\hat{\mathbf{r}}_{ij} \otimes \cdots \otimes \hat{\mathbf{r}}_{ij}}_{\nu_2 \text{ times}} \right) \quad (9)$$

Edge attributes with higher rank can capture more fine-grained directional information. In practice, we typically set $\ell_{\max} = 3$, consistent with common choices in spherical tensor models. Different from cartesian models such as CAMP [17] and HotPP [15] using fully symmetric tensor directly, we further reduce redundant traces, utilizing its highest-weight irreducible components, fully symmetric, traceless Cartesian tensors which serve as the Cartesian analogue of spherical harmonics. The constant here is used to ensure that ${}^{(\nu_2; \nu_2; 1)} \mathbf{E}_{ij}$ can contract to $\hat{\mathbf{r}}_{ij}$ [34]. Here, we employ decomposition matrices to derive ${}^{(\nu_2; \nu_2; 1)} \mathbf{E}_{ij}$ and it can alternatively be constructed via outer products followed by recursive trace subtraction [35].

2.3.7 Atomic basis

We begin by constructing the one particle basis ${}_{p,c}^{\tilde{\nu}_3} \phi_{ij}^{(t)}$ where $\tilde{\nu}_3 \in L_{\max}$ in Eqn. 10 via tensor contraction between node features and edge attributes. Each path is modulated by a learnable radial weight. The particle basis indeed captures pairwise (2-body) interactions at the first layer and higher-body interactions at the rest. The \mathbf{A} -basis in Eqn. 11 is then formed by aggregating the particle basis over neighboring atoms, followed by an optional decomposition to get highest-weight irreducible components. It should be noted that the normalization constant $\mathcal{N}(i)$ can be dynamically determined based on node features, node attributes or edge features, or it can be set according to the average number of neighboring atoms. Our framework also accommodates choice on distinct channels for atomic and product basis construction, while permitting the use of ICTs with $\ell < \tilde{\nu}_3$.

$${}_{p_1, c}^{\tilde{\nu}_3} \phi_{ij}^{(t)} = R_{p_1 c \nu_1 \nu_2 \tilde{\nu}_3}^{(t)}(r_{ij}) \cdot \left({}_c^{\nu_1} \mathbf{h}_i^{(t)} \otimes_R {}^{(\nu_1, \nu_2, \tilde{\nu}_3, p_1)} {}^{(\nu_2; \nu_2; 1)} \mathbf{E}_{ij} \right) \quad (10)$$

$${}_{c}^{\tilde{\nu}_3} \mathbf{A}_i^{(t)} = \frac{1}{\mathcal{N}(i)} \cdot {}^{(\tilde{\nu}_3; \tilde{\nu}_3; 1)} \mathcal{G}_{\triangleright} \left(\sum_{p_1, \tilde{c}} W_{p_1 \tilde{c} \tilde{\nu}_3}^{(t)} \sum_{j \in \mathcal{N}(i)} {}_{p_1, c}^{\tilde{\nu}_3} \phi_{ij}^{(t)} \right) \quad (11)$$

2.3.8 Product basis

Once the atomic basis is obtained, \mathbf{B} -basis in Eqn. 12 can be constructed via self-contraction. The n-correlation ${}^{\nu_3} \mathbf{B}_{i,n}$ where $\nu_3 \in L_{\max}$ is obtained via n times contraction with \mathbf{A} -basis itself. Note that after

every tensor contraction, we could apply an optional decomposition matrix to obtain highest weight.

$${}_{p_2c}^{\nu_3} \mathbf{B}_{i,n}^{(t)} = \underbrace{\bigotimes_{\xi=1}^n ({}_{\tilde{\nu}_3; \xi}^{\nu_3} \mathbf{A}_i^{(t)})}_{\text{with (n-1) times } \mathcal{T}} \quad (12)$$

2.3.9 Message passing

In TACE, the combination of equivariance, path and higher-body-order interactions allows the model to achieve the SOTA accuracy with only two layers (one message passing layers and T=2), outperforming Cartesian models such as CMAP [17] and HotPP [15] typically with T > 2.

$${}_{\tilde{c}}^{\nu_3} \mathbf{h}_i^{(t+1)} = \begin{cases} \sum_{np_2c} W_{np_2cz_i\nu_3}^{(t)} {}_{p_2c}^{\nu_3} \mathbf{B}_{i,n}^{(t)} & \text{if } (t = 0) \text{ and } (T > 1) \\ \sum_{np_2c} W_{np_2cz_i\nu_3}^{(t)} {}_{p_2c}^{\nu_3} \mathbf{B}_{i,n}^{(t)} + \sum_{\tilde{c}} W_{z_i\tilde{\nu}_3\tilde{c}}^{(t)} {}_{\tilde{c}}^{\nu_3} \mathbf{A}_i^{(t)} & \text{if } (t > 0) \text{ or } (T = 1) \end{cases} \quad (13)$$

The node features at layer (t+1) are computed according to Eqn. 13. It is important to note that once the \mathbf{A} and \mathbf{B} basis are constructed, the subsequent feature update involves only learnable linear operations. As a result, the tensor ranks satisfy $\nu_1 = \nu_3 = \tilde{\nu}_3$. Moreover, the first message passing layer lacks self-connections except T = 1, and thus does not incorporate residual links [36]. To enhance the expressive power of the model, we employ coupled features. The TACE framework further provides flexibility to choose between coupled features and element-dependent weights.

2.3.10 Readout

The model predicts short range site energies as a learnable function of the rotationally invariant components of the node features. To preserve the body-order structure inherent in the model. The readout function is kept linear across all but the final layer. In practice, the readout function combines linear neural networks and MLPs, the linear term retains contributions consistent with a body-ordered expansion, while the MLPs capture higher-order interactions from the truncated series. Forces on atoms are obtained via differentiation of the total energy using automatic differentiation. Naturally, the site energy is scaled and shifted, with the specific approach depending on the user's choice.

$$\mathcal{R}^{(t)} \left({}_c^0 h_i^{(t)} \right) = \begin{cases} \sum_c W_c^{(t)} {}_c^0 h_i^{(t)} & \text{if } t < T, \\ \text{MLP} \left({}_c^0 h_i^{(T)} \right) & \text{if } t = T \end{cases} \quad (14)$$

$$E_i^{\text{sr}} = E_i^{\text{ele}} + E_i^{\text{uni}} + \sum_{t=1}^T E_i^{(t)} = E_i^{\text{ele}} + E_i^{\text{uni}} + \sum_{t=1}^T \mathcal{R}^{(t)} \left({}_c^0 h_i^{(t)} \right) \quad (15)$$

For tensors that are directly predicted, such as the dipole moment, polarizability, direct forces, direct stress, and so on, we only need to add a readout corresponding to the appropriate rank. Taking the polarizability as an example, it is constructed from a combination of rank-0 and rank-2 tensors to yield a fully symmetric tensor. Alternatively, in the reducible case, it can be obtained directly using ICTD. Finally, we emphasize that the energy prediction employs the isolated atomic energy either obtained as virtual quantities through least squares fitting or provided directly by the user from DFT calculations as the baseline. In addition, when universal invariant features are available, we can further obtain an optional baseline energy by passing them through a linear layer.

2.3.11 Charges equilibration

In principle, for any node-level rank-0 tensor that must be conserved, the surplus part of the prediction can be uniformly redistributed among atoms. As an illustrative example, we consider the case of atomic charges. While such uniform redistribution is possible, a more physically constrained choice is the Charge Equilibration (Qeq) approach [37, 38]. To this end, we introduce two additional rank-0 readout MLP to predict the electronegativity χ and hardness η (> 0) or $\frac{1}{\eta}$ for each atom. The atomic charges are then obtained by enforcing charge conservation through the following expression:

$$Q_i = \frac{\frac{Q_{\text{tot}} + \sum_i \frac{\chi_i}{\eta_i}}{\sum_i \frac{1}{\eta_i}} - \chi_i}{\eta_i} \quad (16)$$

2.3.12 Latent Ewald Summation

For strict-local and semi-local models based on the short-range approximation, although they are highly effective for most systems, they often exhibit unphysical behavior in systems where long-range interactions are significant, due to neglecting atoms outside the receptive field. Here, we employ the Latent Ewald Summation (LES) as a long-range-correction-drop-in module. For the sake of completeness in model formulation, we briefly outline the principle of LES and its implementation within TACE. Additional details on the implementation and underlying physics can be found in refs. [18–21]. The long-range correction energy for extend system can be formulated as:

$$S(\mathbf{k}) = \sum_{i=1}^N q_i^{\text{les}} e^{i\mathbf{k}\cdot\mathbf{r}_i} \quad (17)$$

$$E^{\text{lr}} = \frac{1}{2\epsilon_0 V} \sum_{0 < k < k_c} \frac{1}{k^2} e^{-\sigma^2 k^2 / 2} |S(\mathbf{k})|^2 \quad (18)$$

where ϵ_0 is the vacuum permittivity, k is the wave vector determined by the cell of the system, k_c is the \mathbf{k} -point cutoff (typically chosen to be π). V is the cell volume, and σ is a smearing factor (typically chosen to be 1 Å). For finite systems, the long-range energy is computed using the pairwise direct sum:

$$E^{\text{lr}} = \frac{1}{2} \frac{1}{4\pi\epsilon_0} \sum_{i=1}^N \sum_{j=1}^N [1 - \varphi(r_{ij})] \frac{q_i^{\text{les}} q_j^{\text{les}}}{r_{ij}} \quad (19)$$

where the complementary error function $\varphi(r) = \text{erfc}(\frac{r}{\sqrt{2}\sigma})$. It should be noted that, depending on the functional form, LES can simultaneously describe both electrostatic and dispersion interactions. Hereafter, the model employing LES as a plugin is referred to as TACE-LES.

Models based on tensors have become widely adopted and extensively studied in recent years, providing a solid foundation for many applications in physics, chemistry, and biology. In contrast, Cartesian tensors, despite their natural and often more straightforward formulation in certain contexts, have not yet been presented in a systematic and comprehensive manner in the existing literature. To address this gap, we begin by reviewing the fundamental concepts of Cartesian tensors (2.2 and 2.3), which serve as the theoretical basis for our approach. We then proceed to describe our method in detail, highlighting its distinguishing features and advantages over existing frameworks.

Table 1: RMSE for energy (E, meV) and forces (F, meV/Å) for the 3BPA dataset. The best-performing results are both **bolded** and underlined.

		GAP[39]	ACE[23]	CACE[16]	Allegro[9]	NequIP[8]	MACE[10]	TACE _{all}	TACE _{max}
300K	E	22.8	7.1	6.3	3.8	3.3	3.0	2.87	<u>2.69</u>
	F	87.3	27.1	21.4	13.0	10.8	8.8	9.84	<u>8.68</u>
600K	E	61.4	24.0	18.0	12.1	11.2	9.7	9.20	<u>8.10</u>
	F	151.9	64.3	45.2	29.2	26.4	21.8	22.59	<u>19.88</u>
1200K	E	166.8	85.3	58.0	42.6	38.5	29.8	31.90	<u>23.42</u>
	F	305.5	187.0	139.6	83.0	76.2	62.0	63.10	<u>54.26</u>
dihedral	E	-	-	-	-	23.2	<u>7.8</u>	13.82	11.00
	F	-	-	-	-	23.1	<u>16.5</u>	18.99	<u>16.45</u>

All models were trained using dataset at T = 300 K. Results for all models except TACE are taken from ref. [16]. Here, both TACE models achieve excellent accuracy. However, note that the use of “all” is merely intended to demonstrate its potential applicability, and does not represent the optimal way of employing it. We only show the performance of “all” here, while all other benchmarks are based on “max”.

2.4 Out-of-Domain — 3BPA

We evaluate the extrapolation capabilities of TACE on the 3-(benzyloxy)pyridin-2-amine (3BPA) dataset, originally introduced in ref. [24], comprises a flexible, drug-like molecule with three rotatable single bonds. The training set consists of 500 geometries sampled from a 300K MD trajectory, which were subsequently reevaluated at the DFT level using the ω B97X exchange-correlation functional and the 6-31G(d) basis set. To assess both in-domain and out-of-domain generalization, three test sets are constructed using MD trajectories at 300K, 600K, and 1200K, respectively. An additional fourth test set consists of dihedral scan geometries, where two dihedral angles are held fixed and the third is systematically varied from 0 to 360 degrees. This results in dihedral slices that sample regions of the PES significantly outside the domain represented by the training data.

Across all splits, TACE attains force and energy RMSE competitive with or better than leading spherical-harmonic equivariant models (NequIP, Allegro, MACE), while using only 64 channels compared to 256 in a comparable MACE baseline (Table 1.). Moreover, the 3BPA dataset is employed in our study to investigate the differences between coupled and uncoupled feature representations in Eqn. 13. We observe that coupled features consistently achieve higher accuracy on force predictions across all test sets. Nonetheless, this result indicates that Cartesian models may achieve higher accuracy with fewer channels when using coupled channel features and if lower-weights can be effectively utilized, the channel can be further reduced.

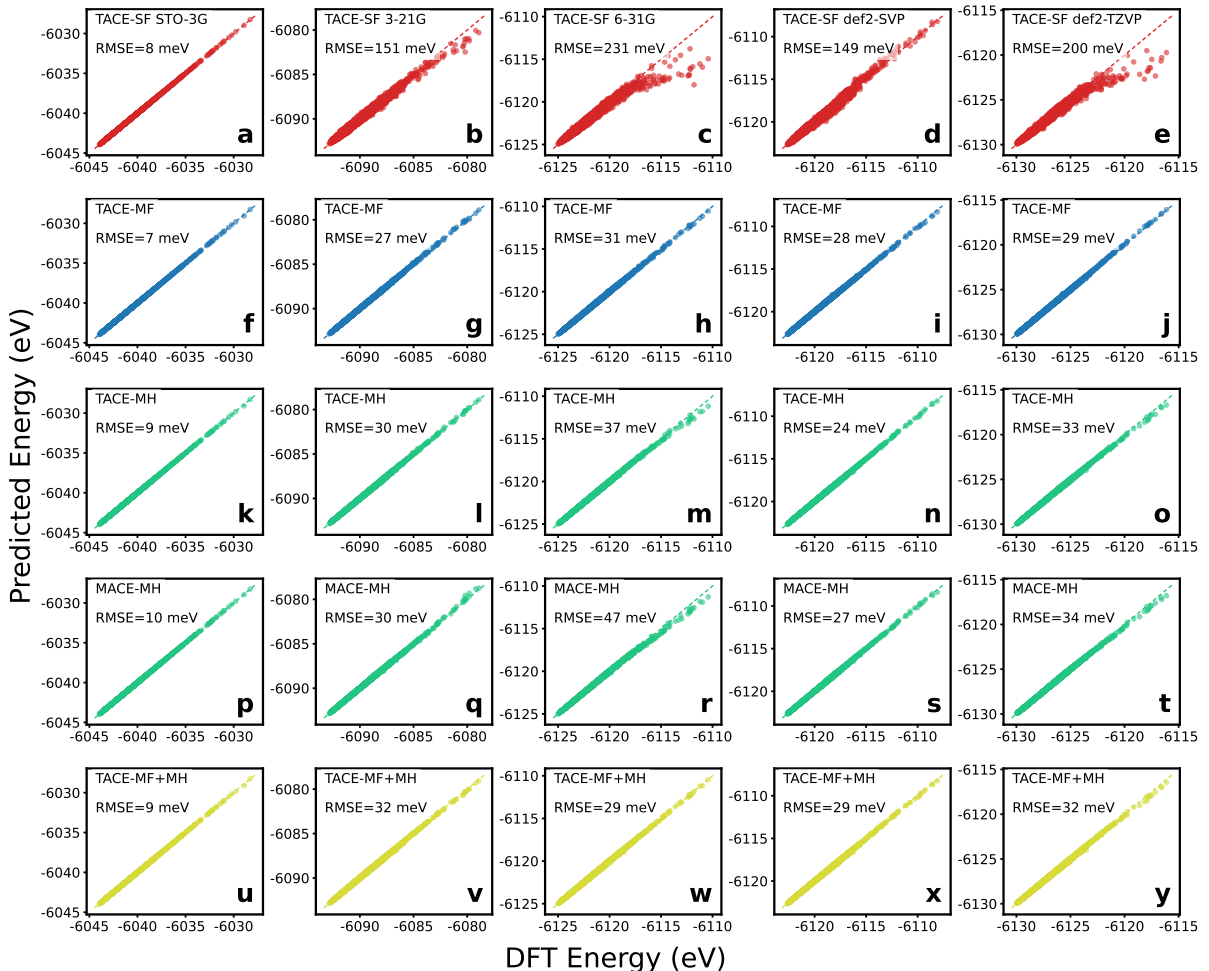


Fig. 2: Comparison of Different Mixed Precision Training Approaches. From left to right, the basis sets are STO-3G, 3-21G, 6-31G, def2-SVP, and def2-TZVP. The test set is the same for each column. **a-e** show TACE using single-fidelity training, **f-j** show TACE using multi-fidelity training, **k-o** show TACE using multi-head training, **p-t** show MACE using multi-head training, **u-y** show TACE using both multi-fidelity and multi-head schemes.

2.5 Mixed Precision Training — Urea

Training on datasets with mixed precision has emerged as an important strategy to reduce the cost of generating high-accuracy reference data. Here, we treat the computational level as an additional discrete label using the universal invariant embedding framework and train TACE on datasets of different electronic-structure fidelities within a single unified model. This strategy, which we refer as multi-fidelity training, differs conceptually from standard multi-head training, implemented in MACE [10, 40]. In multi-head training, separate output heads are attached for each fidelity level while sharing a common representation; in multi-fidelity training, the fidelity label is embodied directly into the representation itself, so that the internal features become level-aware. Both strategies can coexist, but multi-fidelity training offers a more natural route to cross-fidelity generalization.

We evaluate this idea on the QeMFi [41] dataset to compare the effects of single-fidelity (SF), multi-fidelity (MF), multi-head (MH), and their combined approaches on predictive performance. The dataset contains 15,000 molecular configurations for each of five levels, computed using TD-DFT with the CAM-B3LYP functional. The basis sets, in order of increasing accuracy, are: STO-3G, 3-21G, 6-31G, def2-SVP, and def2-TZVP. A large low-fidelity dataset supplemented with a small amount of high-fidelity data: STO-3G serves as the baseline with a train:validation:test split of 41:9:50, while the other levels use a split of 1:9:90, so that only a very small amount of the total training data comes from the higher levels. Single-fidelity models are trained using datasets from only one basis set, whereas other models are trained on a combined dataset incorporating all five fidelity levels. As shown in Fig. 2, the red region indicates that, for the high-fidelity dataset, the model trained solely on limited high-fidelity data fails to generalize to unseen configurations. In contrast, both multi-fidelity and multi-head training greatly reduce these errors as high-fidelity supervision is now supported by abundant low-fidelity structures. Multi-fidelity TACE achieves the lowest errors across high-energy configurations, outperforming both the multi-head variant of TACE and the multi-head MACE baseline under matched architectures and hyperparameters. This improvement mainly arises from use of coupled features, which improves accuracy under the same channel size. Although the yellow region in Fig. 2 does not show a significant advantage from combining multi-head and multi-fidelity schemes, this combination still provides a more flexible modeling option. It is also worth noting that the introduction of high-fidelity data may slightly degrade the accuracy on low-fidelity datasets, but the gain at the high-fidelity levels is substantial. Overall, these experiments demonstrate that universal embeddings let TACE act as a cross-fidelity learner.

Table 2: RMSE for energy per atom (E, meV/atom) and forces (F, meV/Å) for the 32-water system. The best-performing results are highlighted in both **bold** and underline.

	Invariant Models				Equivariant Models			MACE [10]		TACE	
	BPNN[3]	DeepPMD[42]	ACE[24]	REANN[5]	NequIP[8]	CACE[16]	CAMP[17]	64-0	192-2	64-0	64-2
E	2.3	2.1	1.7	0.8	0.9	0.6	0.59	0.6	0.6	0.58	0.72
F	120	92	99	53	45	47	34	37.1	36.2	33.16	30.31

Results for all models except TACE are taken from refs. [17, 43]. Here, 64-0 denotes $c = 64$ and $L_{\max} = 0$.

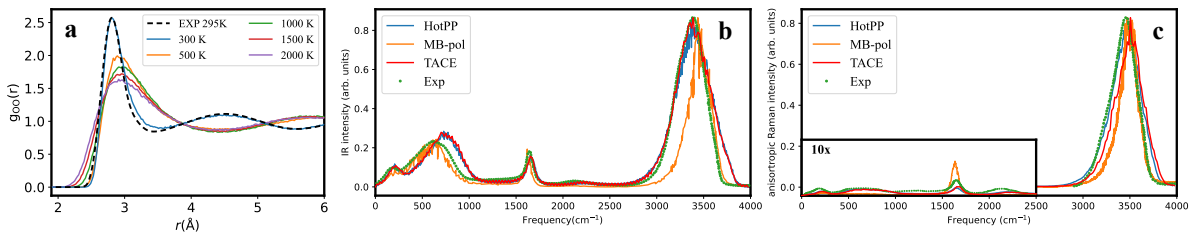


Fig. 3: Water simulation outcomes with $L_{\max} = 0$. **a** O-O RDFs at different temperatures from NVT MD simulations and X-ray diffraction. **b** IR spectra. **c** Raman spectra.

Table 3: Relative RMSE, defined as the RMSE normalized by the intrinsic standard deviation of the validation set (RRMSE, %) for dipole moment (D) and polarizability (α) across different water systems. For each training set size, the best-performing results are highlighted in both **bold** and underline.

System		$N_{\text{train}} = 500$				$N_{\text{train}} = 700$	
		SA-GPR[44]	REANN[5]	TNEP[45]	TACE	HotPP[15]	TACE
monomer	D	0.11	0.05	0.069	0.008	0.02	0.006
	α	0.02/0.12	0.06	5.89/1.22	0.086	0.05	0.042
dimer	D	5.3	3.0	1.681	0.521	2.36	0.372
	α	6.4/7.8	1.6	8.82/12.59	2.644	0.99	2.058
zundel	D	2.4	0.4	0.371	0.049	0.15	0.046
	α	3.8/0.97	0.1	1.20/1.06	0.129	0.09	0.090
liquid water	D	-	15	0.852	1.260	0.7	0.959
	α	5.8/19	2.1	16.28/20.38	5.898	0.48	5.303

Results for all models except TACE are taken from refs. [15, 45]. For polarizability, some models predict the $\ell = 0$ and $\ell = 2$ components individually, and their errors are given as values separated by a slash. In this benchmark, we report errors on the validation set in accordance with previous studies.

2.6 Liquid water: structure, dynamics, and spectra

We assess the performance of TACE on liquid water using a dataset of 1593 configurations labeled at the revPBE0-D3 level [46], which is known to provide a reliable description of the structure and dynamics of water across a range of pressures and temperatures [47]. Listed in Table 2, TACE attains the lowest RMSE of energy per atom and forces, comparing against invariant models (BPNN and DeepMD [3, 7]), linear ACE-style models, and recent equivariant message-passing models (NequIP, MACE and CAMP [8, 10, 17]). Notably, similar to ref. [43], a small-scale TACE model with invariant messages ($L_{\text{max}} = 0$) already outperforms top-performing models, indicating that the irreducible Cartesian framework is highly data-efficient and does not require large, high-rank tensor channels to reach state-of-the-art accuracy.

We then test whether this accuracy translates into physically correct dynamics and performed three independent 300-ps simulations of bulk water at 300 K, 500 K, 1000 K, 1500 K, and 2000 K using the $L_{\text{max}} = 0$ model. The O-O radial distribution function (RDF) is shown in Fig. 3 (a). At 300 K, the calculated RDF agrees remarkably well with experimental results [48]. We also computed the mean square displacement (MSD) and obtained the diffusion coefficient using the Einstein relation, yielding $0.26(1), 1.58(1), 3.17(7), 4.66(7), 5.90(28) \times 10^{-5} \text{ cm}^2/\text{s}$ at 300, 500, 1000, 1500, 2000K, which is in excellent consistency with the AIMD value of $2.67 \times 10^{-5} \text{ cm}^2/\text{s}$ in 300K [49]. The TACE potential maintains stable MD simulations up to 2000 K, highlighting its robustness.

A central goal of this work is to explore whether TACE can simultaneously and accurately predict both scalar and tensorial properties. We therefore investigate whether TACE can describe dipole moments and polarizabilities of various water systems, and reproduce the infrared and Raman spectra of liquid water. For the dipole moment, we directly predict a vector $\nu = 1$. For the polarizability, since it is a traceless and fully symmetric tensor, we predict two components: the trace part ($\ell = 0$) and the traceless fully symmetric part ($\ell = 2$). The prediction accuracy is reported in terms of the relative RMSE [44] in Table 3 and the explicit formula can be found in ref. [50]. TACE achieved very high accuracy in predicting dipole moments, achieving the best performance in three of the four systems considered, and shows competitive polarizability accuracy overall. However, some anomalous values can be observed in the Table 3, despite its strong performance across other systems. We believe that this is due to the fact that the polarizability labels are not true symmetric tensors; instead, they are constructed from the instantaneous dielectric tensor using the tensorial extension of Clausius-Mossotti relation [51]. HotPP fits it as a reducible Cartesian tensor by predicting a generic rank-2 tensor, which is later symmetrized, and includes an additional scalar corresponding to the diagonal element. By contrast, our model enforces full tensor symmetry by explicitly summing the $\ell = 0$ and $\ell = 2$ components. Thus, the slightly higher polarizability error is therefore best understood as a limitation of dataset labels [44] due to intrinsic noise, not of the representation itself.

To obtain the infrared and Raman spectra, we employed an NPT-equilibrated configuration of 512 water molecules from ref. [15]. This was followed by an additional 100 ps equilibration in the NVT

ensemble using TACE trained on the dataset of ref. [52]. Subsequently, three production simulations were carried out in the NVE ensemble, each with a duration of 200 ps. Throughout all simulations, a time step of 0.5 fs was applied. The infrared and Raman spectra were then obtained by performing Fourier transforms of the respective autocorrelation functions. From Fig. 2, we can see that our computed results are in good agreement with experiments. The Raman spectrum shows a slight blue shift in the high-frequency region, which can also be attributed to the non-strict symmetry of the polarizability labels. At the same time, our spectra were obtained without applying broadening. It should be emphasized that quantum effects in water can significantly influence both the RDF and the simulated spectra, as demonstrated in refs. [47, 53–55]. Overall, our model achieves excellent performance in both stability and accuracy, while also demonstrating TACE’s effective simulation of scalars, tensors, and spectra.

Table 4: RMSE for energy (E, meV/atom) and forces (F, meV/Å) for the GAP17 dataset. The best-performing results are both **bolded** and underlined.

	GAP[39]	MTP[4]	REANN[5]	NEP[56]	NequIP[8]	HotPP[15]	TACE
E	46	35	31	42	17	16	8.55
F	1100	630	640	690	431	395	299.88

Results for all models except TACE are from refs. [15, 56].

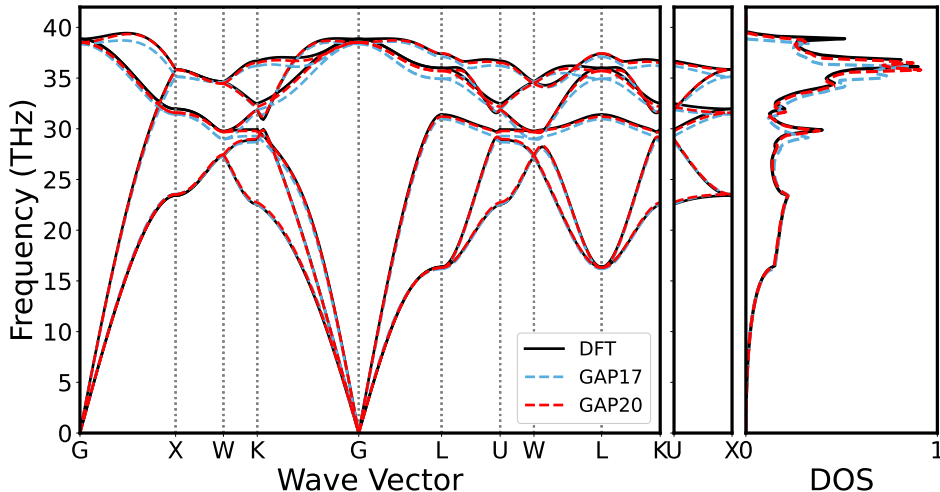


Fig. 4: Phonon Spectrum of Diamond. Phonon dispersion relations of diamond predicted by TACE models trained on the GAP17 [57] and GAP20 [58] datasets, compared with DFT results [15].

2.7 Hessians — GAP17 and GAP20

Accurate prediction of higher-order derivatives by the MLIP is crucial for phonon behavior, as the curvature of the true PES around equilibrium points directly determines the phonon frequencies and dispersion. We benchmarked on the GAP17 dataset [57] contains configurations representing a variety of carbon allotropes. On this dataset, TACE achieves an energy RMSE of 8.55 meV/atom and forces RMSE of 299.88 meV/Å, substantially outperforming other models in (Table 4). Accurate modeling of vibrational properties has historically posed challenges for carbon systems in ref. [58]. To directly assess curvature quality, we compute phonon dispersions for diamond from the TACE potential, following the same protocol used in ref. [15], and Phonopy [59, 60] to generate the phonon spectrum. As illustrated in Fig. 4, the phonon branches predicted by TACE agree well with DFT across the Brillouin zone. By contrast, we noticed that HotPP [15] model trained on the GAP17 dataset, reported noticeable discrepancies in the high-frequency region near the Γ -point. To enable a more detailed comparison, we retrained our model using the more accurate and comprehensive GAP20 dataset [58], generated with

the optB88-vdW. The resulting phonon spectrum is in near-perfect agreement with DFT calculations, confirming that TACE can reproduce both forces and second-derivative information across lower-level and higher-level DFT datasets.

Table 5: RMSE for energy (E, meV/atom), forces (F, meV/Å), stress (S, Gpa) and magnetic forces (F_{mag} , meV/ μ_{B}) for FeAl dataset. The best-performing results are highlighted in both **bold** and underline.

	mMTP ¹ [61]	mMTP ¹ [61]	mTACE
E	1.61	1.73	<u>0.62</u>
F	63.01	64.4	<u>7.60</u>
S	0.45	0.469	<u>0.08</u>
F_{mag}	15.4	15.2	<u>3.71</u>

¹The results of mMTP correspond to magnetic basis = 4 and 5, respectively.

2.8 Magnetic systems — FeAl

Magnetic materials present a particular challenge for MLIPs because, in addition to the 3N atomic positional degrees of freedom that define a conventional potential energy surface, they also carry 3N spin degrees of freedom associated with local magnetic moments. MagNet [62] first utilized magnetic forces (i.e., the negative gradient of energy with respect to magnetic moments) as training labels. These advances now enable more thorough studies of magnetic systems.

Leveraging the universal embedding framework, we extend TACE to mTACE, which treats per-atom magnetic moments as explicit vector-valued features and learns their interactions on the same footing as structural degrees of freedom. We evaluate mTACE on a FeAl binary system generated in ref.[61], as listed in Table 5. Beyond quantitative accuracy, mTACE is in principle capable of predicting formation energies and lattice parameters, reproducing thermal expansion behavior, and capturing total magnetic moments even at high Al concentrations, while ensuring robust structural and magnetic relaxations.

Table 6: MAE for electric enthalpy (U, meV/atom), forces (F, meV/Å), stress (S, meV/Å³), polarization (P, me · Å/atom), polarizability (α , me · Å² · V⁻¹) and Born effective charges (BEC, me) for BaTiO₃. For models trained with 59 configurations, the best-performing results are highlighted in both **bold** and underline.

	$N_{\text{train}} = 59$			$N_{\text{train}} = 75$
	FITACE	Allegro-pol-ZBL	FITACE-ZBL	Allegro-pol [63]
U	0.32	0.46	<u>0.25</u>	0.5
F	<u>13.93</u>	27.6	14.10	14.6
S	0.13	0.43	<u>0.12</u>	-
P	0.39	1.74	<u>0.33</u>	1.4
α	43.09	45.3	<u>39.13</u>	15.2
BEC	<u>13.71</u>	21.2	13.73	14.1

Results for Allegro-pol trained with 75 configurations are taken from the official paper [63], and it is unclear whether ZBL (Ziegler-Biersack-Littmark) potentials [22] were used. All other models were trained by us using the publicly available 59 configurations, while Allegro-pol was trained using the official input files. For the 59-configuration models, we explicitly indicate whether ZBL was applied.

2.9 External field — BaTiO₃

Modeling ferroelectric perovskites such as BaTiO₃ under external electric fields is challenging for first-principles methods. To assess whether TACE can learn such field-coupled responses, we use its field-embedded variant (FITACE), which incorporates the external electric field as an equivariant through the universal embedding framework.

We trained FITACE with the BaTiO₃ dataset introduced in ref. [63], which consists of 59 frames extracted from MD simulations in the limit of zero electric field. We compare the unified model with the benchmark results (see Table 6), and FITACE achieves greater accuracy due to its architecture and semi-local nature. This indicates that our framework is capable of faithfully reproducing various physical properties under external electric fields. When we additionally include a short-range ZBL term (FITACE-ZBL), the accuracy further improves and remains competitive with, or better than, Allegro-pol trained on a larger set of 75 configurations. These results indicate that the universal embedding framework makes TACE extendable, with minimal modification, to systems under external electric fields.

2.10 Charged systems

We evaluate charge-aware learning on the dataset constructed by Ko et al. [38], which includes structures in various charge states where long-range electrostatics and charge transfer are decisive. Ag trimers with total charge of +1 and -1, ionic Na₉Cl₈ clusters formed by the removal of a neutral Na atom, carbon chains terminated with hydrogen atoms in both neutral and positively charged states, and a periodic system consisting of a gold cluster adsorbed on a MgO(001) slab.

Utilizing the universal embedding framework, energy and forces were benchmarked to illustrate the effects of including charges and total charge embeddings and the charge errors correspond to models trained jointly on energy, forces, and charge labels. All models, except ACE [23] and CACE-LR [19], use LES or charge embeddings, either explicitly embedding charges or using charges as labels. Overall, the results are highly satisfactory, shown in Table 7. One notable exception is the Ag systems, where our approach does not show a clear advantage in energy prediction. As long as embedding charges are used, incorporating the total charge as a continuous variable or omitting it has little effect on the error. We suspect this may be due to an inadequate embedding strategy for the total charge, a relatively low weight assigned to the energy term in the loss function, or possibly because competing models are overfitting, as suggested by the consistently low forces errors of our model.

Table 7: RMSE for energy (E, meV/atom), forces (F, meV/Å) and charges (Q, me) for different charged systems. The best-performing results are highlighted in both **bold** and underline.

System		ACE[23]	$\chi + \eta(\text{ACE})$ [64]	3G-HDNNP[65]	4G-HDNNP[38]	CACE-LR[21]	TACE
C ₁₀ H ₂ /C ₁₀ H ₃ ⁺	E	0.76	0.75	2.045	1.194	0.73	0.21
	F	37.22	35.16	231.0	78.00	36.9	2.13
	Q	-	2.000	-	6.577	-	0.58
Ag ₃ ^{+/-}	E	809.62	0.21	320.2	1.323	0.162	2.54
	F	285.81	23.10	1913	31.69	29.0	12.22
	Q	-	0.415	-	9.976	-	0.46
Na _{8/9} Cl ₈ ⁺	E	1.55	0.71	2.042	0.481	0.21	0.55
	F	41.72	12.35	76.67	32.78	9.78	1.06
	Q	-	7.020	-	15.830	-	1.40
Au ₂ -MgO(001)	E	2.56	1.63	-	0.219	0.073	1.18
	F	88.70	50.27	-	66.00	7.91	3.82
	Q	-	3.340	-	5.698	-	1.93

Results for all models except TACE are taken from refs. [21, 38, 64].

2.11 Advantages and Limitations of ACE — REICO-AgPdCHO

Prior benchmarks use well-established databases designed to probe fundamental E/F/S potential energy surfaces or specific physical embeddings. These datasets most contains high-symmetry MD-derived structures which often clusters around near-equilibrium state, on which, as we shown, TACE achieves very high accuracy. Beside what we already shown, MLIP also also pursue generality, which is governed to a

Table 8: Average distances of main chain carbon, carboxylic oxygen, and anhydride oxygen atoms from the Ag(111) surface (in Å).

	uMLIPs						finetune		from-scratch	
	EXP [66]	DFT [67]	OrbV3 con-inf	7Net MF-omat	MACE OMAT-medium	NequIP OAM-L	Allegro OAM-L	MACE OMAT-medium	NequIP RECIO[68]	TACE LES
main chain carbon	2.86	2.97	3.38	3.22	3.21	3.73	3.51	3.00	2.98	2.97
carboxylic oxygen	2.66	2.67	3.07	3.03	3.40	3.29	2.79	2.72	2.68	2.69
anhydride oxygen	2.98	2.85	3.18	3.15	3.51	3.37	3.02	2.99	2.92	2.86
MAE	-	-	0.38	0.30	0.54	0.63	0.28	0.07	0.03	0.01

The benchmark result of the TACE model was obtained with a batch size of 16 at the 216th epoch and MAE are compared against DFT.

Table 9: Energy barriers (eV) for CO oxidation on various PdAg surfaces. Failures in searching TS are indicated by ×.

System	DFT [68]	uMLIPs				finetune		from-scratch	
		OrbV3 con-inf	MACE OMAT-medium	NequIP OAM-L	Allegro OAM-L	MACE OMAT-medium	NequIP RECIO[68]	TACE LES	
Pd100	0.63	0.60	0.66	0.65	0.88	0.69	0.67	0.65	
Pd110	0.69	0.64	0.69	0.55	0.56	0.70	0.79	0.67	
Pd111	1.39	×	×	×	×	×	1.35	1.29	
Pd-TB	0.86	0.71	1.04	1.03	1.02	1.17	0.91	1.12	
Pd-cube	1.28	1.01	1.17	1.17	1.35	1.23	1.18	1.23	
Pd-S/Ag(111)	0.42	0.46	×	×	×	×	0.42	0.38	
Pd-line/Ag(111)	0.55	×	×	0.64	×	0.51	0.58	0.51	
Pd ₁ /Ag(111)	0.28	0.27	×	0.40	0.31	×	0.38	0.29	
Pd ₄ /Ag(111)	0.23	×	0.28	×	0.32	×	0.21	0.20	
Pd ₉ /Ag(111)	0.87	×	×	×	×	×	0.73	0.87	
Pd ₁₃ /Ag(111)	0.74	×	0.36	×	0.60	0.45	0.60	0.54	
Pd ₂₀ /Ag(111)	0.90	0.69	0.89	0.85	0.76	0.92	0.99	0.91	
MAE	-	0.11	0.11	0.10	0.15	0.11	0.07	0.07	

The benchmark result of the TACE model was obtained with a batch size of 16 at the 216th epoch and MAE are compared against DFT.

large extent by the chemical-space diversity of the training data. Recent efforts such as RECIO [68] sampling learns from randomized structures, reducing dependence on preselected configuration manifolds and pushing MLIPs toward DFT-like generality; likewise, recent new public datasets like OMat24[69], also emphasizes non-equilibrium coverage. Yet while such non-standard or non-system-specific data broaden coverage, they also raise the bar for training. On the AgPdCHO dataset [68], for example, ACE-based models often require extensive hyperparameter tuning; otherwise training can exhibit a spontaneous RMSE rise and eventually fail (even when customized metric scaling or Huber loss is applied). By contrast, NequIP trained reliably across most settings, suggesting an architecture-data interaction rather than a purely data issue. We hypothesize that the randomly generated structures are hard to be simultaneously captured well lack enough physical constraints, which leads to conflicts with the strong inductive biases of ACE-based frameworks. In practice, we also observe that two-layer ACE-based models can, in some cases, become more sensitive to outliers.

As a solution, we integrate LES as a plug-in long-range correction, which supplies appropriate physical constraints, that are especially helpful for models with short receptive fields, while remaining fully compatible with TACE’s design. With LES add-on, TACE can effectively learn from the complex datasets generated by the RECIO method, overcoming the inherent limitation of ACE framework. We benchmark the TACE trained AgPdCHO EMLP(element-based machine learning potentials) with selected test cases from the original work that are representative in heterogeneous catalysis, including adsorption of PTCDA on Ag(111) (Table 8.), CO oxidation on various PdAg surfaces (Table 9), and Acetylene hydrogenation on Pd(111), H covered Pd(111) and AgPd alloys (Table 10), Baker reaction (see SI Table S1). We employed the Atomic Simulation Environment package [70] to perform the following structure optimizations and transition state (TS) searches. We have also included the latest uMLIP (MACE-OMAT-medium [40], OrbV3-conservative-inf-omat [71], 7Net-omat [72], NequIP-OAM-L, Allegro-OAM-L [73]) and fine-tuned MACE-OMAT-medium with REICO data for comparison. Overall, we find TACE delivers the most balanced, zero-shot performance among all models, sub-0.03 Å deviations for PTCDA/Ag(111) adsorption

Table 10: Energy barriers (eV) for various Pd(111) and PdAg surfaces with different adsorbates. Failures in searching TS are indicated by \times .

System	DFT [68]	uMLIPs				finetune		from-scratch	
		OrbV3 con-inf	MACE OMAT	NequIP OAM-L	Allegro OAM-L	MACE OMAT	NequIP RECIO[68]	TACE LES	
Pd(111)-C ₂ H ₃	0.87	0.72	0.74	0.74	0.55	0.78	0.73	0.79	
Pd(111)-C ₂ H ₄	0.79	0.70	0.76	0.68	0.68	0.72	0.74	0.71	
Pd(111)-C ₂ H ₅	0.79	0.67	0.61	0.63	\times	0.74	0.73	0.85	
Pd(111)-C ₂ H ₆	0.71	\times	0.50	0.44	0.54	0.53	0.76	0.70	
1 ML-Pd(111)-C ₂ H ₃	0.67	\times	0.72	0.75	\times	\times	0.74	0.36	
1 ML-Pd(111)-C ₂ H ₄	0.69	0.65	0.65	0.65	0.57	0.64	0.62	0.57	
1 ML-Pd(111)-C ₂ H ₅	0.90	\times	0.60	0.67	0.59	0.72	0.64	0.75	
1 ML-Pd(111)-C ₂ H ₆	0.45	0.45	0.39	0.56	0.39	0.45	0.42	0.48	
0.25 ML-PdAg ₃ (111)-C ₂ H ₃	0.58	\times	0.61	0.62	\times	0.60	0.51	0.63	
0.25 ML-PdAg ₃ (111)-C ₂ H ₄	0.37	0.59	0.52	0.48	0.51	0.47	0.44	0.43	
0.25 ML-PdAg ₃ (111)-C ₂ H ₅	0.42	0.67	0.61	0.66	0.62	0.68	0.71	0.62	
0.25 ML-PdAg ₃ (111)-C ₂ H ₆	0.17	0.33	\times	0.34	0.28	0.25	0.35	0.32	
1 ML-PdAg(111)-C ₂ H ₃	0.58	0.52	0.52	0.53	0.43	0.52	0.48	0.49	
1 ML-PdAg(111)-C ₂ H ₄	0.36	\times	0.67	0.42	0.70	0.45	0.43	0.35	
1 ML-PdAg(111)-C ₂ H ₅	0.79	0.78	0.67	0.66	0.65	0.72	0.46	0.70	
1 ML-PdAg(111)-C ₂ H ₆	0.36	0.44	0.41	0.50	0.40	0.39	0.46	0.45	
MAE	-	0.11	0.13	0.13	0.17	0.09	0.12	0.10	

The benchmark result of the TACE model was obtained with a batch size of 16 at the 216th epoch and MAE are compared against DFT.

distances, MAE \approx 0.07 eV for CO-oxidation barriers across diverse Pd/PdAg with 100% TS success, and within \leq 0.1 eV of DFT across coverage/alloy conditions. We verified the reliability of the predicted TS geometries by confirming their structural correctness and ensuring that each valid TS exhibited exactly one imaginary frequency (as the Hessians were available, frequencies could be obtained either by finite-difference calculations or by diagonalization after coordinate transformation, with the latter introducing less numerical noise). For OrbV3-conservative-inf-omat, the model failed to obey the appropriate physical constraints. As a result, the models may encounter issues such as energy non-conservation in the NVE ensemble [74], failure to locate transition state pathways [75], or even extremely unusual and completely incorrect optimization trajectories (e.g., adsorption optimization of PTCDA using OrbV3-direct-inf; see SI Fig. S2). It is also interesting to see the fine-tuned MACE-OMAT did not yield consistent gains and, in some cases, underperformed its pretrained counterpart. Our preliminary conclusion is that the conflict between ACE and RECIO persists, the randomized RECIO data contain a higher fraction of distributional outliers, which can confuse the model and degrade generalization.

2.12 uMLIP — TACE-MatPES

Here, we demonstrate the extrapolative capabilities of our model using a relatively small uMLIP dataset. In this case, we restrict the product basis with “ $\nu_1 \leq \nu_2$ ” to further improve computational efficiency, and we train two types of models: an element-aware model and an element-agnostic model. Apart from the element-dependent part in the product basis, the rest of the architecture is kept identical. During the training of the element-aware model, we observed that its performance on the shear modulus test was more sensitive to the presence of outliers. After a certain number of epochs, although the overall accuracy continued to improve, abnormal values appeared for a few outlier samples. For fairness, we did not filter out these test results. Instead, we defined the best epoch as the point occurring within the first 20% of epochs before such outliers began to emerge. For consistency, we adopted the exact same data partitioning scheme as used in the MatPES publications [76] of CHGNet [77], M3GNet [78], and TensorNet [14]. Using this setup, we evaluate the performance of the TACE-MatPES and compare its results on more comprehensive benchmarks. It can be seen that, whether using a small-parameter model or an extremely large-parameter model, we achieve superior results. Notably, TACE offers great flexibility in controlling model parameters; for model covering 89 elements, it allows us to freely choose between 1M and 30M parameters, and even smaller or larger parameter counts are permissible. For further comparisons regarding model size, hyperparameters, and speed, please refer to SI 2.1.

Table 11: MAE for energy per atom (E, meV), forces (F, meV/Å), stress (S, GPa), structural similarity (d), formation energy per atom (E_f , meV/atom), bulk modulus (K_{VRH} , GPa), shear modulus (G_{VRH} , GPa) and constant-volume heat capacity (C_v , $\text{J} \cdot \text{mol}^{-1} \cdot \text{K}^{-1}$). Off-equilibrium forces ($\frac{F}{F_{\text{DFT}}}$). Number of sarameters. (\uparrow/\downarrow) stands for higher/lower the better. The best-performing results are highlighted in both **bold** and underline.

MatPES-PBE						
	M3GNet [78]	CHGNet ¹ [77]	TensorNet [14]	TACE Element-Agnostic ² [10]	TACE ³	TACE Element-Aware
E ↓	-	-	-	35	...	<u>31</u>
F ↓	45	<u>31</u>	36	105	...	<u>101</u>
S ↓	181	136	148	0.655	...	<u>0.607</u>
d ↓	0.888	0.642	0.700	0.39	...	0.38
E_f ↓	0.42	0.43	<u>0.37</u>	80	...	<u>72</u>
K_{VRH} ↓	110	82	81	17	...	<u>16</u>
G_{VRH} ↓	26	24	18	15	...	<u>13</u>
C_v ↓	25	21	15	12	...	<u>11</u>
$\frac{F}{F_{\text{DFT}}}$ ↑	27	23	13	0.93	...	0.94
Parameters	<u>0.97</u>	0.91	0.93	0.93	...	0.94
	0.66M	2.70M	0.84M	0.98M	...	29.8M

¹CHGNet includes magmoms information. So there will be better performance in terms of energy.

²We follow MACE in the naming of model modules. “Element-Agnostic” indicates that the parameters of this module (product basis here) do not depend on the elements. The results of MACE-MATPES-PBE-0 are not included here, as the model was pretrained on OMat24 and subsequently finetuned, with the MatPES dataset further subjected to an additional filtering step.

³The ellipsis indicates that we can flexibly adjust the number of parameters by changing the size of the hidden channels and by choosing whether or not to include element dependence, ranging from 0.98M to 29.8M.

We do not run MD benchmarks for this, as they can only be run by the Materials Virtual Lab.

3 Discussion

In our view, the most effective form of equivariance arises from tensor product operations (irreducible Cartesian tensor products/contractions, $SO(3)/SO(2)$ spherical tensor products, and a series of other derived methods developed to accelerate computations). For the work presented in this paper, we believe that the effectiveness and accuracy of Cartesian models have already been well demonstrated. However, we also see current limitations in the implementation of irreducible Cartesian tensor products/contractions, and hereby discuss the future road-map.

Regarding the irreducible Cartesian tensor products/contractions, present implementation typically forms tensor products over all valid combinations (ν_1, ν_2, ν_o , not path here) and then extracts the highest-weight irreducible component via ICTD. In contrast, a single path spherical tensor product can generate multiple irreducible components; importantly, Cartesian tensors can also yield multiple irreducible components from a single tensor product/contraction. As illustrated in SI Fig. S3, the 3^ν elements in a Cartesian tensor are not entirely redundant; they allow other irreducible components with different weights to be generated from a single tensor product/contraction. The specific implementation approach has already been outlined in Fig. 1a. Consider a rank- ν Cartesian tensor with weight $\nu - 1$. Such a tensor has 3^ν components, but only $2\nu - 1$ of them are useful. In principle, one can project with ICTD, map to spherical irreps (retaining the $2\nu - 1$ nonzeros), then reassemble a rank- $(\nu - 1)$ Cartesian tensor of weight $(\nu - 1)$. Although we have not yet implement this pathway, we will improve this part based on e3nn in the future and anticipate this approach to embed richer radial information, reduce path count, thus, improve both accuracy and speed.

Beyond the ideal route above, we have employed ICTD in two ways: the first is “max”, which uses only the highest weight for a given rank; the second is “all”, which utilizes all available weights. For the “max” approach, we do not elaborate further here. In the “all” case, we do not directly embed radial weights along the path; however, each path is still modulated by a learnable weight initialized to 1.0. Instead, after tensor product, the messages obtained on each edge are processed via ICTD, at which point radial information is embedded through $\sum_{\ell,q} R_{\ell,q} \cdot^{(\nu;\ell;q)} \mathbf{T}$. In other words, the number of radial weights depends on the rank of the tensor rather than the possible path. The “all” strategy does not necessarily yield better performance, as it is not our optimal implementation. Nonetheless, pairing a weight ℓ with a learnable radial weight is a natural and straightforward approach. Finally, we emphasize that our tensor product operations do not require the input tensors to be irreducible, reducible cases can be handled in a unified manner.

Further speedups are available via compilation and kernel libraries. In current benchmarks (see SI 2.1), TACE is about half as fast as Cuda-accelerated MACE(v0.3.14). The current Cartesian framework does have ample potentials: removing the product basis and using layers with $T > 2$ (plus optional gating, i.e., a NequIP-like Cartesian architecture) yields significant speedups; even without acceleration, TACE ($T > 2$, correction=1) is comparable to compiled NequIP(v0.15.0), while retaining an atomic basis and the functionality discussed above.

SO(2)-style simplification in Cartesian space. It is known that SO(2) spherical tensor products significantly simplify computational cost, making L_{\max} or $\ell_{\max} = 6$ feasible. In Cartesian space, it may be advantageous to use symmetric edge attributes. For example, if we rotate all edges to the direction $[1, 0, 0]$ (i.e., along the x -axis), then fully symmetric edge attributes with a trace will have only a single nonzero element. This implies that tensor products could effectively reduce to simple indexing and scaling operations. However, in our experiments, we found that the speed did not significantly improve, since contraction steps with rotation matrices are required for both the node features and the output features. Moreover, because the edge attributes used here are symmetric and not strictly equivalent to the SO(2) spherical tensor products, further improvement may be needed in the future.

$$(\mathbf{E}_{ij})_{i_1 i_2 \dots i_n} = \frac{(2\nu_2 - 1)!!}{\nu_2!} \cdot \prod_{k=1}^{\nu_2} \delta_{i_k, 0}, \quad (20)$$

The gradient of the Cartesian tensor product is simple. Since the Cartesian tensor product does not involve Clebsch-Gordan coefficients, the tensor product can be reduced to simple matrix multiplication. Therefore, its gradient is very simple. Denoting the upstream gradient as G , the gradients with respect to input A and B during backpropagation are given as in Eqn. 21. By extension, arbitrary-order derivatives can be obtained. However, in our experiments, explicitly writing out the first analytical gradient did not lead to a speedup. This may be because PyTorch’s native optimizations are already efficient, or because our implementation still operates entirely within PyTorch without leveraging other backends. Nevertheless, it is possible that future developments could theoretically take better advantage of this property.

$$\nabla_A = GB^\top \quad \nabla_B = A^\top G \quad (21)$$

Hybrid designs are also viable, for example, applying Cartesian tensor products with spherical representations. In the future, we will also introduce Cartesian-3j and Cartesian-nj to explore some new possibilities.

4 Conclusion

In this work, we present a unified design approach for Cartesian models and, based on this irreducible Cartesian tensor product/contraction method, implement TACE, an E(3)-equivariant (or SE(3)) message-passing framework built upon higher-order Cartesian tensors that operates directly in Cartesian space. TACE accommodates tensors of arbitrary rank and both reducible or irreducible Cartesian tensors. The framework can consistently extract the corresponding irreducible components of different weight, allowing us to freely extract and manipulate them. Furthermore, the model is capable of directly predicting tensorial properties, and through the use of a universal embedding, we can flexibly incorporate and control various factors (both invariants and equivariants) influencing the predicted physical quantities. Although we only demonstrate external fields, magnetic moments, charges, and fidelities here, the framework can be readily extended. Taken together, these results suggest that a Cartesian framework such as TACE can serve as the backbone of next-generation MLIPs, applicable across a broad range of problems in chemistry and physics and it is reasonable to expect that MLIPs of this style will become the primary computational engine for routine atomistic simulation and property prediction.

5 Methods

Software

All experiments were conducted using the TACE software available at <https://github.com/xvzemin/tace> and Python version 3.12.11. The TACE-MatPES model was trained using PyTorch 2.8.0+cu128 and PyTorch Lightning 2.5.5, while all other results were obtained based on PyTorch 2.6.0+cu124 and

PyTorch Lightning 2.5.2. For other models, we use orb-models 0.5.2, mace-torch 0.3.12(uMLIP), mace-torch 0.3.14(urea and speed test), cuequivariance 0.3.0, sevens 0.11.1.dev2, allegro-pol 0.0.3 and nequip 0.15.0. In addition, most of the plotting relies on Matplotlib [79].

Bechmarks

3BPA: For the 3BPA dataset, we also utilize a 5 Å cutoff [24]. The training set contains 500 structures, with 10% reserved for validation. Testing is performed on four separate subsets corresponding to temperatures of 300 K, 600 K, 1200 K, and a dihedral scan, comprising 1,669; 2,138; 2,139; and 7,047 structures, respectively.

Water: For the liquid water dataset [46], a cutoff of 6 Å is applied. Following the protocol used in CAMP [17], the dataset is split into 1,432 configurations for training, 79 for validation, and 81 for testing. The dipole moment (μ) and polarizability (α) for various water systems were taken from ref. [44]. Values of μ and α for molecules such as H_2O , $(\text{H}_2\text{O})_2$, and H_5O_2^+ were calculated using the coupled cluster singles and doubles (CCSD) method with the d-aug-cc-pVTZ basis set. For liquid water, the dataset was generated using the Perdew-Burke-Ernzerhof (PBE) exchange-correlation functional together with ultrasoft pseudopotentials (USPPs). A cutoff of 6 Å was employed for training the dipole and polarizability models, except for $(\text{H}_2\text{O})_2$, for which a cutoff of 10 Å was used. The training and validation splits were either 500:500 or 700:300. The dataset employed for IR and Raman simulations comprises 1,888 structures calculated using the strongly constrained and appropriately normed (SCAN) functional. Our model attains a RMSE of 2.43meV/atom for energy, 30.97meV/Å for forces, and 1.00 meV/atom for virials. The train-test split follows the TNEP scheme [45], with 1,510 structures used for training and 378 for testing, and an additional 10% of the training set reserved for validation. The MD system simulated consists of 512 water molecules, corresponding to a density of 1 g/cm³. A time step of 1 fs was employed, and temperature control is maintained using a Nosé-Hoover thermostat.

GAP17 and GAP20: In the GAP17 dataset [57], a 5 Å cutoff is used. The training subset includes 4,080 structures, with 10% held out for validation purposes, while the test set contains 450 configurations. Similarly, the GAP20 dataset [58] applies the same cutoff, with a total of 6088 structures in dataset. Of these, 10% are used for validation and an additional 10% for testing.

BaTiO₃: The BaTiO₃ dataset was generated via active learning from MD simulations in the temperature range of 300-400 K. The original Allegro-pol [63] model was reported to be trained with 75 configurations. However, only 59 configurations are available in their public GitHub repository. Therefore, we retrained the model using these 59 configurations for a fair comparison. The training followed a protocol similar to the official setup, employing a cutoff radius of 6 Å, with 47 configurations used for training and 12 for validation. Model performance was evaluated on the validation set. The dataset was computed at the PBE level under a small external electric field of 0.36 MV·cm⁻¹, and the final reference data correspond to extrapolation to the zero-field limit.

Charges: The datasets for different charge states and charge-transfer systems [38] were generated using the PBE functional with a light computational setting. Spin-polarized calculations were performed for the Au₂-MgO, NaCl, and Ag₃ systems. The Ag, NaCl, carbon-chain, and Au₂-MgO datasets contain 11,013, 5,000, 10,019, and 5,000 structures, respectively. For each dataset, 10% of the configurations were used as the validation set, and all reported errors are evaluated on the validation set. For the charge embedding benchmarks of the Ag, NaCl, carbon-chain, and Au₂-MgO systems, the cutoff radii are 5.29, 5.29, 4.23, and 5.5 Å, respectively. When using charges together with energy and forces as training labels, the corresponding cutoff values are 6.0, 6.0, 4.23, and 6.0 Å, respectively.

Urea: For this dataset, our model uses a fully unified set of parameters. Even in single-fidelity training, the model incorporates basis set labels, with a uniform cutoff of 5 Å.

FeAl: The dataset contains a total of 2632 bcc FeAl configurations, of which 85% are non-equilibrium magnetic configurations (i.e., with nonzero magnetic forces) obtained from constrained DFT calculations using the PBE functional. We adopt a cutoff of 6 Å. Since mMTP [61] employed 5-fold cross-validation, we follow a similar data-splitting scheme, with a train-to-validation ratio of 0.8:0.2.

PdAgCHO: PdAgCHO dataset was generated using the RECIO method [68] and contains a total of 116,516 structures. For fine-tuning, 100,000 structures were randomly selected, while the remaining configurations were used for validation. For from-scratch training, we use all structures, and the learning rate scheduler adopts warmup followed by cosine annealing. All structures were computed at the PBE level. The fine-tuning models and TACE models was carried out by us with a uniform cutoff of 6 Å. It should be noted that the NequIP [8] model was not trained by us, and that the dataset partitioning scheme employed in NequIP differs from ours.

MatPES: The MatPES dataset [76] was generated for uMLIPs, with calculations performed under both PBE and r2SCAN functionals. In this work, we only use the PBE subset and adopt the same data splitting scheme as in the original publication.

Training details

All models are trained on a single RTX 4090 GPU, and if the memory is insufficient, a single A800 GPU is used instead. For all training, edge attributes were truncated at $l_{\max} = 3$, and the number of layers was set to $T = 2$. All models were trained with either the 64-0 or 64-2 (channel- L_{\max}) configuration, except for rMD17, which employed the 128-2 setting. Each combination was restricted to a single path, and the number of channels c in both the atomic basis and the product basis was kept identical. The radial basis was constructed with 8 or 10 functions, which could be either fixed or trainable depending on the model setting. For the radial embedding, the MLP architecture was chosen as [64, 64, 64] or [64, 64, 64, 1024]. The SiLU activation function was consistently applied to all nonlinear operations. All models were optimized using Adam [80] with the AMSGrad variant [81], together with the ReduceLROnPlateau learning-rate scheduler implemented in PyTorch [82] and pytorch-cosine-annealing-with-warmup for PdAgCHO. The loss function is defined as the weighted sum of the mean squared errors (MSE) for energy per atom, forces, virials, with task-specific weighting hyperparameters and huber loss for TACE-MatPES. For more detailed hyperparameters see SI Table S5.

Data availability

Although multiple random seeds were not used in this study for efficiency, most tests were performed with seed = 42. We ensure that all results are fully reproducible. All datasets will be made available on GitHub <https://github.com/xvzemin/tace-fit>.

Code availability

The implementation of TACE will be made available on GitHub <https://github.com/xvzemin/tace> and uMLIPs training on OMat24 and several other datasets will also be released soon.

Acknowledgements

The authors thank Bin Jiang, Junfan Xia, Chenyu Wu, Changxi Yang, Junjie Wang and Shihao Shao for fruitful discussions. This work was supported by the National Natural Science Foundation of China NSFC (22433004 and 22403064) and ShanghaiTech University.

Author contribution

P.H., D.X. and W.X. conceived the project and guided the research the project. The TACE code, equations, figures, tables and benchmark results were prepared by Z.X. All authors edited and revised the manuscript.

Competing interests

The authors declare no competing interests.

References

- [1] Fu, X. *et al.* Learning smooth and expressive interatomic potentials for physical property prediction (2025). [arXiv:2502.12147](https://arxiv.org/abs/2502.12147).
- [2] Riebesell, J. *et al.* A framework to evaluate machine learning crystal stability predictions. *Nature Machine Intelligence* **7**, 836–847 (2025).
- [3] Behler, J. & Parrinello, M. Generalized neural-network representation of high-dimensional potential-energy surfaces. *Phys. Rev. Lett.* **98**, 146401 (2007).
- [4] Shapeev, A. V. Moment tensor potentials: A class of systematically improvable interatomic potentials. *Multiscale Modeling & Simulation* **14**, 1153–1173 (2016).
- [5] Zhang, Y., Xia, J. & Jiang, B. Physically motivated recursively embedded atom neural networks: Incorporating local completeness and nonlocality. *Physical Review Letters* **127**, 156002 (2021).
- [6] Schütt, K. *et al.* Guyon, I. *et al.* (eds) *Schnet: A continuous-filter convolutional neural network for modeling quantum interactions*. (eds Guyon, I. *et al.*) *Advances in Neural Information Processing Systems*, Vol. 30 (Curran Associates, Inc., 2017).
- [7] Wang, H., Zhang, L., Han, J. & E, W. Deepmd-kit: A deep learning package for many-body potential energy representation and molecular dynamics. *Computer Physics Communications* **228**, 178–184 (2018).
- [8] Batzner, S. *et al.* E(3)-equivariant graph neural networks for data-efficient and accurate interatomic potentials. *Nature Communications* **13**, 2453 (2022).
- [9] Musaelian, A. *et al.* Learning local equivariant representations for large-scale atomistic dynamics. *Nature Communications* **14**, 579 (2023).
- [10] Batatia, I., Kovács, D. P., Simm, G. N. C., Ortner, C. & Csányi, G. Mace: Higher order equivariant message passing neural networks for fast and accurate force fields. *arXiv preprint* (2023).
- [11] Passaro, S. & Zitnick, C. L. Reducing so(3) convolutions to so(2) for efficient equivariant gnns (2023). [arXiv:2302.03655](https://arxiv.org/abs/2302.03655).
- [12] Snider, R. F. *Irreducible Cartesian Tensors* (De Gruyter, Berlin, Boston, 2018).
- [13] Zaverkin, V. *et al.* Higher-rank irreducible cartesian tensors for equivariant message passing (2024).
- [14] Simeon, G. & Fabritiis, G. d. TensorNet: Cartesian tensor representations for efficient learning of molecular potentials (2023).
- [15] Wang, J. *et al.* E(n)-equivariant cartesian tensor message passing interatomic potential. *Nature Communications* **15**, 7607 (2024).
- [16] Cheng, B. Cartesian atomic cluster expansion for machine learning interatomic potentials. *npj Computational Materials* **10**, 157 (2024).
- [17] Wen, M., Huang, W.-F., Dai, J. & Adhikari, S. Cartesian atomic moment machine learning interatomic potentials. *npj Computational Materials* **11**, 128 (2025).
- [18] Cheng, B. Latent ewald summation for machine learning of long-range interactions. *npj Computational Materials* **11**, 80 (2025).
- [19] Kim, D., King, D. S., Zhong, P. & Cheng, B. Learning charges and long-range interactions from energies and forces. *arXiv preprint arXiv:2412.15455* (2024).
- [20] Zhong, P., Kim, D., King, D. S. & Cheng, B. Machine learning interatomic potential can infer electrical response. *arXiv preprint arXiv:2504.05169* (2025).

- [21] Kim, D. *et al.* A universal augmentation framework for long-range electrostatics in machine learning interatomic potentials. *arXiv preprint arXiv:2507.14302* (2025).
- [22] Ziegler, J. F. & Biersack, J. P. *The Stopping and Range of Ions in Matter* (Springer US, 1985).
- [23] Drautz, R. Atomic cluster expansion for accurate and transferable interatomic potentials. *Phys. Rev. B* **99**, 014104 (2019).
- [24] Kovács, D. P. *et al.* Linear atomic cluster expansion force fields for organic molecules: Beyond rmse. *Journal of Chemical Theory and Computation* **17**, 7696–7711 (2021).
- [25] Bochkarev, A., Lysogorskiy, Y. & Drautz, R. Graph atomic cluster expansion for semilocal interactions beyond equivariant message passing. *Phys. Rev. X* **14**, 021036 (2024).
- [26] Batatia, I. *et al.* The design space of e(3)-equivariant atom-centred interatomic potentials. *Nature Machine Intelligence* **7**, 56–67 (2025).
- [27] Coope, J. A. R., Snider, R. F. & McCourt, F. R. Irreducible cartesian tensors. *The Journal of Chemical Physics* **43**, 2269–2275 (1965).
- [28] Andrews, D. L. & Ghoul, W. A. Irreducible fourth-rank cartesian tensors. *Physical Review A* **25**, 2647–2657 (1982).
- [29] Bonvicini, A. Irreducible cartesian tensor decomposition: A computational approach. *The Journal of Chemical Physics* **160**, 224105 (2024).
- [30] Shao, S., Li, Y., Lin, Z. & Cui, Q. High-rank irreducible cartesian tensor decomposition and bases of equivariant spaces. *Journal of Machine Learning Research* **26**, 1–53 (2025).
- [31] Geiger, M. *et al.* Euclidean neural networks: e3nn (2022).
- [32] Vinod, V. & Zaspel, P. Benchmarking data efficiency in Δ -ml and multifidelity models for quantum chemistry. *The Journal of Chemical Physics* **163**, 024134 (2025).
- [33] Gasteiger, J., Groß, J. & Günnemann, S. Directional message passing for molecular graphs (2020).
- [34] Applequist, J. Traceless cartesian tensor forms for spherical harmonic functions: new theorems and applications to electrostatics of dielectric media. *Journal of Physics A: Mathematical and General* **22**, 4303 (1989).
- [35] Toth, V. T. & Turyshev, S. G. Efficient trace-free decomposition of symmetric tensors of arbitrary rank. *International Journal of Geometric Methods in Modern Physics* **19**, 2250201 (2022).
- [36] He, K., Zhang, X., Ren, S. & Sun, J. Deep residual learning for image recognition. *arXiv preprint arXiv:1512.03385* (2015).
- [37] Rappe, A. K. & Goddard, W. A. I. Charge equilibration for molecular dynamics simulations. *The Journal of Physical Chemistry* **95**, 3358–3363 (1991).
- [38] Ko, T. W., Finkler, J. A., Goedecker, S. & Behler, J. A fourth-generation high-dimensional neural network potential with accurate electrostatics including non-local charge transfer. *Nature Communications* **12**, 398 (2021).
- [39] Bartók, A. P., Payne, M. C., Kondor, R. & Csányi, G. Gaussian approximation potentials: The accuracy of quantum mechanics, without the electrons. *Phys. Rev. Lett.* **104**, 136403 (2010).
- [40] Batatia, I. *et al.* A foundation model for atomistic materials chemistry (2024). [arXiv:2401.00096](https://arxiv.org/abs/2401.00096).
- [41] Vinod, V. & Zaspel, P. QeMFi: A multifidelity dataset of quantum chemical properties of diverse molecules. *Scientific Data* **12**, 202 (2025).

- [42] Wang, H., Zhang, L., Han, J. & E, W. Deepmd-kit: A deep learning package for many-body potential energy representation and molecular dynamics. *Computer Physics Communications* **228**, 178–184 (2018).
- [43] Kovács, D. P., Batatia, I., Arany, E. S. & Csányi, G. Evaluation of the mace force field architecture: From medicinal chemistry to materials science. *The Journal of Chemical Physics* **159**, 044118 (2023).
- [44] Grisafi, A., Wilkins, D. M., Csányi, G. & Ceriotti, M. Symmetry-adapted machine learning for tensorial properties of atomistic systems. *Phys. Rev. Lett.* **120**, 036002 (2018).
- [45] Xu, N. *et al.* Tensorial properties via the neuroevolution potential framework: Fast simulation of infrared and raman spectra. *Journal of Chemical Theory and Computation* **20**, 3273–3284 (2024).
- [46] Cheng, B., Engel, E. A., Behler, J., Dellago, C. & Ceriotti, M. Ab initio thermodynamics of liquid and solid water. *Proceedings of the National Academy of Sciences* **116**, 1110–1115 (2019).
- [47] Marsalek, O. & Markland, T. E. Quantum dynamics and spectroscopy of ab initio liquid water: The interplay of nuclear and electronic quantum effects. *The Journal of Physical Chemistry Letters* **8**, 1545–1551 (2017).
- [48] Skinner, L. B., Benmore, C. J., Neufeind, J. C. & Parise, J. B. The structure of water around the compressibility minimum. *The Journal of Chemical Physics* **141**, 214507 (2014).
- [49] Marsalek, O. & Markland, T. E. Quantum dynamics and spectroscopy of ab initio liquid water: The interplay of nuclear and electronic quantum effects. *The Journal of Physical Chemistry Letters* **8**, 1545–1551 (2017).
- [50] Zhang, Y. *et al.* Efficient and accurate simulations of vibrational and electronic spectra with symmetry-preserving neural network models for tensorial properties. *The Journal of Physical Chemistry B* **124**, 7284–7290 (2020).
- [51] Talebian, E. & Talebian, M. A general review on the derivation of clausius–mossotti relation. *Optik* **124**, 2324–2326 (2013).
- [52] Zhang, L., Wang, H., Car, R. & E, W. Phase diagram of a deep potential water model. *Physical Review Letters* **126**, 236001 (2021).
- [53] Kapil, V., Wilkins, D. M., Lan, J. & Ceriotti, M. Inexpensive modeling of quantum dynamics using path integral generalized langevin equation thermostats. *The Journal of Chemical Physics* **152** (2020).
- [54] Shepherd, S., Lan, J., Wilkins, D. M. & Kapil, V. Efficient quantum vibrational spectroscopy of water with high-order path integrals: From bulk to interfaces. *The Journal of Physical Chemistry Letters* (2021).
- [55] Kapil, V., Kovács, D. P., Csányi, G. & Michaelides, A. First-principles spectroscopy of aqueous interfaces using machine-learned electronic and quantum nuclear effects. *Faraday Discussions* **249**, 50–68 (2024).
- [56] Fan, Z. *et al.* Gpumd: A package for constructing accurate machine-learned potentials and performing highly efficient atomistic simulations. *The Journal of Chemical Physics* **157**, 114801 (2022).
- [57] Deringer, V. L. & Csányi, G. Machine learning based interatomic potential for amorphous carbon. *Phys. Rev. B* **95**, 094203 (2017).
- [58] Rowe, P., Deringer, V. L., Gasparotto, P., Csányi, G. & Michaelides, A. An accurate and transferable machine learning potential for carbon. *The Journal of Chemical Physics* **153**, 034702 (2020).

- [59] Togo, A. First-principles phonon calculations with phonopy and phono3py. *Journal of the Physical Society of Japan* **92**, 012001 (2023).
- [60] Togo, A., Chaput, L., Tadano, T. & Tanaka, I. Implementation strategies in phonopy and phono3py. *Journal of Physics: Condensed Matter* **35**, 353001 (2023).
- [61] Kotykhov, A. S. *et al.* Fitting to magnetic forces improves the reliability of magnetic moment tensor potentials. *Computational Materials Science* **245**, 113331 (2024).
- [62] Yuan, Z. *et al.* Equivariant neural network force fields for magnetic materials. *Quantum Frontiers* **3**, 8 (2024).
- [63] Falletta, S. *et al.* Unified differentiable learning of electric response. *Nature Communications* **16**, 4031 (2025).
- [64] Rinaldi, M., Bochkarev, A., Lysogorskiy, Y. & Drautz, R. Charge-constrained atomic cluster expansion. *Phys. Rev. Mater.* **9**, 033802 (2025).
- [65] Yao, K., Herr, J. E., Toth, D. W., Mckintyre, R. & Parkhill, J. The tensormol-0.1 model chemistry: a neural network augmented with long-range physics. *Chem. Sci.* **9**, 2261–2269 (2018).
- [66] Hauschild, A. *et al.* Normal-incidence x-ray standing-wave determination of the adsorption geometry of ptcda on ag(111): Comparison of the ordered room-temperature and disordered low-temperature phases. *Phys. Rev. B* **81**, 125432 (2010).
- [67] Ruiz, V. G., Liu, W., Zojer, E., Scheffler, M. & Tkatchenko, A. Density-functional theory with screened van der waals interactions for the modeling of hybrid inorganic-organic systems. *Phys. Rev. Lett.* **108**, 146103 (2012).
- [68] Yang, C., Wu, C., Xie, W., Xie, D. & Hu, P. General reactive element-based machine learning potentials for heterogeneous catalysis. *Nature Catalysis* **8**, 891–904 (2025).
- [69] Barroso-Luque, L. *et al.* Open materials 2024 (omat24) inorganic materials dataset and models (2024). [arXiv:2410.12771](https://arxiv.org/abs/2410.12771).
- [70] Hjorth Larsen, A. *et al.* The atomic simulation environment—a python library for working with atoms. *Journal of Physics: Condensed Matter* **29**, 273002 (2017).
- [71] Rhodes, B. *et al.* Orb-v3: atomistic simulation at scale (2025). [arXiv:2504.06231](https://arxiv.org/abs/2504.06231).
- [72] Park, Y., Kim, J., Hwang, S. & Han, S. Scalable parallel algorithm for graph neural network interatomic potentials in molecular dynamics simulations. *J. Chem. Theory Comput.* **20**, 4857–4868 (2024).
- [73] Tan, C. W. *et al.* High-performance training and inference for deep equivariant interatomic potentials (2025). [arXiv:2504.16068](https://arxiv.org/abs/2504.16068).
- [74] Bigi, F., Langer, M. & Ceriotti, M. The dark side of the forces: assessing non-conservative force models for atomistic machine learning (2025). [arXiv:2412.11569](https://arxiv.org/abs/2412.11569).
- [75] Zhao, Q. *et al.* Harnessing machine learning to enhance transition state search with interatomic potentials and generative models. *Advanced Science* **12**, e06240 (2025).
- [76] Kaplan, A. D. *et al.* A foundational potential energy surface dataset for materials (2025). [arXiv:2503.04070](https://arxiv.org/abs/2503.04070).
- [77] Deng, B. *et al.* CHGNet as a pretrained universal neural network potential for charge-informed atomistic modelling. *Nature Machine Intelligence* **5**, 1031–1041 (2023).
- [78] Chen, C. & Ong, S. P. A universal graph deep learning interatomic potential for the periodic table. *Nature Computational Science* **2**, 718–728 (2022).

- [79] Hunter, J. D. Matplotlib: A 2d graphics environment. *Computing in Science & Engineering* **9**, 90–95 (2007).
- [80] Kingma, D. P. & Ba, J. Adam: A method for stochastic optimization (2017). [arXiv:1412.6980](https://arxiv.org/abs/1412.6980).
- [81] Reddi, S. J., Kale, S. & Kumar, S. On the convergence of adam and beyond (2019).
- [82] Paszke, A. *et al.* Pytorch: An imperative style, high-performance deep learning library (2019).